Physics results from the first COHERENT observation of coherent elastic neutrino-nucleus scattering in argon and their combination with cesium-iodide data

M. Cadeddu,[1,†] F. Dordei,[1,‡] C. Giunti,[2,§] Y. F. Li,[3,4,‖] E. Picciau,[5,6,¶] and Y. Y. Zhang[3,4,*]

[1]*Istituto Nazionale di Fisica Nucleare (INFN), Sezione di Cagliari, Complesso Universitario di Monserrato—S.P. per Sestu Km 0.700, 09042 Monserrato (Cagliari), Italy*
[2]*Istituto Nazionale di Fisica Nucleare (INFN), Sezione di Torino, Via P. Giuria 1, I-10125 Torino, Italy*
[3]*Institute of High Energy Physics, Chinese Academy of Sciences, Beijing 100049, China*
[4]*School of Physical Sciences, University of Chinese Academy of Sciences, Beijing 100049, China*
[5]*Dipartimento di Fisica, Università degli Studi di Cagliari, and INFN, Sezione di Cagliari, Complesso Universitario di Monserrato—S.P. per Sestu Km 0.700, 09042 Monserrato (Cagliari), Italy*
[6]*University of Massachusetts, Amherst, Massachusetts 01003, USA*

(Received 5 May 2020; accepted 15 July 2020; published 31 July 2020)

We present the results on the radius of the neutron distribution in ^{40}Ar, on the low-energy value of the weak mixing angle, and on the electromagnetic properties of neutrinos obtained from the analysis of the coherent neutrino-nucleus elastic scattering data in argon recently published by the COHERENT Collaboration, taking into account proper radiative corrections. We present also the results of the combined analysis of the COHERENT argon and cesium-iodide data for the determination of the low-energy value of the weak mixing angle and the electromagnetic properties of neutrinos. In particular, the COHERENT argon data allow us to improve significantly the only existing laboratory bounds on the electric charge $q_{\mu\mu}$ of the muon neutrino and on the transition electric charge $q_{\mu\tau}$.

DOI: 10.1103/PhysRevD.102.015030

I. INTRODUCTION

The observation of coherent elastic neutrino-nucleus scattering (CEνNS) in cesium iodide performed in 2017 by the COHERENT experiment [1,2] unlocked an innovative and powerful tool to study many and diverse physical phenomena [3–12]. Recently, the COHERENT Collaboration observed CEνNS for the first time also in argon [13], using a single-phase 24 kg liquid-argon (LAr) scintillation detector, with two independent analyses that prefer CEνNS over the background-only null hypothesis with greater than 3σ significance. The experimental challenge behind this analysis is the need to observe nuclear recoils with a very small kinetic energy $T_{\rm nr}$ of a few keV, and thus the need of a low nuclear-recoil-energy threshold, in the presence of a larger background, when compared to the cesium-iodide case. This requirement is necessary for the coherent recoil of the nucleus which occurs for $|\vec{q}|R \ll 1$ [14], where $|\vec{q}| \simeq \sqrt{2MT_{\rm nr}}$ is the three-momentum transfer, R is the nuclear radius of a few fm, and M is the nuclear mass, of about 40 GeV for argon nuclei. The observation in argon, which is the lightest nucleus for which the CEνNS process has been measured, allows one to demonstrate the CEνNS cross-section dependence on the square of the number of neutrons N^2, but it can also provide valuable information on nuclear physics, neutrino properties, physics beyond the standard model (SM), and electroweak (EW) interactions.

In this paper, we present the bounds on different parameters of the EW interaction and neutrino electromagnetic properties obtained analyzing the new COHERENT Ar data and those obtained with a combined analysis of the COHERENT Cesium iodide (CsI) and Ar data, using the results of the analysis of the CsI data in Ref. [15]. During the completion of this work, another analysis of this type appeared on arXiv [16], but the results are not comparable with ours because we fit the COHERENT Ar data, whereas the analysis of Ref. [16] is not a fit of the COHERENT Ar data, but a fit of the number of CEνNS events obtained by the COHERENT Collaboration from

*Corresponding author.
zhangyiyu@ihep.ac.cn
†matteo.cadeddu@ca.infn.it
‡francesca.dordei@cern.ch
§carlo.giunti@to.infn.it
‖liyufeng@ihep.ac.cn
¶emmanuele.picciau@ca.infn.it

the fit of the data [13]. Such an indirect analysis underestimates the systematic uncertainties, especially those due to the background that are not taken into account.

The plan of the paper is as follows. In Sec. II we describe briefly the CEνNS formalism used in our calculation as well as the inputs employed for simulating the signal spectra. In Secs. III and IV we derive, respectively, the results on the average rms radius of the neutron distributions in Ar and on the weak mixing angle. In Secs. V, VI, and VII we present, respectively, the constraints on the neutrino charge radii, neutrino electric charges, and magnetic moments. Finally, in Sec. VIII we summarize the results of the paper.

II. FORMALISM AND SIGNAL PREDICTIONS

The SM weak-interaction differential cross section as a function of the nuclear kinetic recoil energy $T_{\rm nr}$ of CEνNS processes with a spin-zero nucleus $\mathcal{N}$ with Z protons and N neutrons is given by [17–19]

$$\frac{d\sigma_{\nu_\ell-\mathcal{N}}}{dT_{\rm nr}}(E,T_{\rm nr}) = \frac{G_{\rm F}^2 M}{\pi}\left(1-\frac{MT_{\rm nr}}{2E^2}\right)[g_V^p Z F_Z(|\vec{q}|^2)+g_V^n N F_N(|\vec{q}|^2)]^2, \tag{1}$$

where $G_{\rm F}$ is the Fermi constant, $\ell = e, \mu, \tau$ is the neutrino flavor, and E is the neutrino energy. The well-known tree-level values of g_V^p and g_V^n are

$$g_V^p = \frac{1}{2} - 2\sin^2\vartheta_W, \qquad g_V^n = -\frac{1}{2}, \tag{2}$$

where $\vartheta_{\rm W}$ is the weak mixing angle, also known as the Weinberg angle. In this paper we consider the following more accurate values that take into account radiative corrections in the $\overline{\rm MS}$ scheme [20]:

$$g_V^p(\nu_\ell) = \rho\left(\frac{1}{2}-2\sin^2\vartheta_W\right) - \frac{\hat{\alpha}_Z}{4\pi\hat{s}_Z^2}\left(1-2\frac{\hat{\alpha}_s(m_W)}{\pi}\right) + \frac{\alpha}{6\pi}\left(3-2\ln\frac{m_\ell^2}{m_W^2}\right), \tag{3}$$

$$g_V^n = -\frac{\rho}{2} - \frac{\hat{\alpha}_Z}{8\pi\hat{s}_Z^2}\left(7-5\frac{\hat{\alpha}_s(m_W)}{\pi}\right), \tag{4}$$

where

$$\sin^2\vartheta_W = 0.23857 \pm 0.00005\,[21] \tag{5}$$

is the low-energy value of the weak mixing angle, often denoted with $\hat{s}_0^2$ [20,21], and

$$\rho = 1.00058\,[21], \tag{6}$$

$$\hat{s}_Z^2 = 0.23122 \pm 0.00003\,[21], \tag{7}$$

$$\hat{\alpha}_Z^{-1} = 127.955 \pm 0.010\,[21], \tag{8}$$

$$\hat{\alpha}_s(m_W) = 0.123 \pm 0.018 \pm 0.017\,[22] \tag{9}$$

are, respectively, the ρ parameter of electroweak interactions, the value of $\sin^2\vartheta_W$ at the scale of the Z-boson mass, the value of the electromagnetic fine-structure constant at the scale of the Z-boson mass, and the value of the strong constant at the scale of the W-boson mass. The value of $\hat{\alpha}_s(m_W)$ in Eq. (9) is the only measured one that we found in the literature. It is in agreement with the PDG summary in Fig. 9.5 of Ref. [21]. In any case, a precise value of $\hat{\alpha}_s(m_W)$ is not needed, because its contribution is practically negligible.

The terms in Eqs. (3) and (4) proportional to $\hat{\alpha}_Z/\hat{s}_Z^2$, which in turn is proportional to the square of the charged-current weak coupling constant, are due to box diagrams with W-boson propagators. The last term in Eq. (3) depends on the flavor ℓ of the interacting neutrino ν_ℓ through the corresponding charged lepton mass m_ℓ. This term can be interpreted as the contribution of the neutrino charge radius and is consistent with the expression of the neutrino charge radius calculated in Refs. [23–25] that we will discuss in Sec. V.

Numerically, neglecting the small uncertainties, we obtain

$$g_V^p(\nu_e) = 0.0401, \tag{10}$$

$$g_V^p(\nu_\mu) = 0.0318, \tag{11}$$

$$g_V^n = -0.5094. \tag{12}$$

These values are different from the tree-level values $g_V^p = 0.0229$ and $g_V^n = -0.5$ obtained with Eq. (2), especially those of $g_V^p(\nu_e)$ and $g_V^p(\nu_\mu)$.

In Eq. (1) $F_Z(|\vec{q}|^2)$ and $F_N(|\vec{q}|^2)$ are, respectively, the form factors of the proton and neutron distributions in the nucleus. They are given by the Fourier transform of the corresponding nucleon distribution in the nucleus and describe the loss of coherence for $|\vec{q}|R_p \gtrsim 1$ and $|\vec{q}|R_n \gtrsim 1$, where R_p and R_n are, respectively, the rms radii of the proton and neutron distributions. For the two form factors one can use different parametrizations. The three most popular ones are the symmetrized Fermi [26], Helm [27], and Klein-Nystrand [28] parametrizations that give practically identical results, as we have verified (see Fig. 2). Here, we briefly describe only the Helm parametrization (descriptions of the other parametrizations can be found in several papers, for example in Refs. [3,26,29,30]) that is given by

$$F^{\mathrm{Helm}}(q^2) = 3\frac{j_1(qR_0)}{qR_0}e^{-q^2s^2/2}, \tag{13}$$

where $j_1(x) = \sin(x)/x^2 - \cos(x)/x$ is the spherical Bessel function of order one and R_0 is the box (or diffraction) radius. The rms radius R of the corresponding nucleon distribution is given by

$$R^2 = \frac{3}{5}R_0^2 + 3s^2. \tag{14}$$

For the parameter s that quantifies the so-called surface thickness, we consider the value $s = 0.9$ fm which was determined for the proton form factor of similar nuclei [31].

We determined the value of the rms proton distribution radius R_p from the value of the ^{40}Ar charge radius measured precisely in electromagnetic experiments [32,33],

$$R_c = 3.4274 \pm 0.0026 \text{ fm}. \tag{15}$$

The charge radius R_c is given by [34,35][1]

$$R_c^2 = (R_p^{\mathrm{point}})^2 + \langle r_p^2\rangle + \frac{N}{Z}\langle r_n^2\rangle_c, \tag{16}$$

where R_p^{point} is the point-proton distribution radius, $\langle r_p^2\rangle^{1/2} = 0.8414 \pm 0.0019$ fm [36] is the charge radius of the proton, and $\langle r_n^2\rangle_c = -0.1161 \pm 0.0022$ fm^2 is the squared charge radius of the neutron [21]. Since the proton form factor $F_Z(|\vec{q}|^2)$ in the cross section in Eq. (1) describes only the interaction of the protons in the nucleus, the corresponding proton distribution radius R_p is given by

$$R_p^2 = (R_p^{\mathrm{point}})^2 + \langle r_p^2\rangle = R_c^2 - \frac{N}{Z}\langle r_n^2\rangle_c. \tag{17}$$

From the experimental value of R_c in Eq. (15), we obtain

$$R_p = 3.448 \pm 0.003 \text{ fm}. \tag{18}$$

This is the value of the rms radius R_p that we used in our calculations.

Let us now consider the neutron distribution radius R_n that determines the neutron form factor $F_N(|\vec{q}|^2)$ in the cross section in Eq. (1). Experimentally, the value of R_n is not known, and we can get information on it from the fit of the COHERENT data, as discussed in Sec. III. However, in our analysis it would be unphysical to consider R_n as a completely free parameter, because it is very plausible that the neutron distribution radius is larger than the proton distribution radius R_p in Eq. (18) [37], since the ^{40}Ar nucleus has 22 neutrons and only 18 protons. In order to check if this hypothesis is supported by the nuclear theory, we have calculated the proton and neutron radii with two publicly available numerical codes: the Sky3D code [38] of nonrelativistic nuclear mean-field models based on Skyrme forces, and the DIRHB code [39] of relativistic self-consistent mean-field models. Table I presents the results of the calculation of the point-proton radius R_p^{point} and point-neutron radius R_n^{point} for different nuclear interactions (the codes can calculate only the point-nucleon distributions that do not take into account the finite size of the nucleons). From Table I one can see that $R_n^{\mathrm{point}} > R_p^{\mathrm{point}}$ in all the nuclear models that we have considered and the excess is between 0.08 and 0.11 fm. Since

TABLE I. Values of the ^{40}Ar point-proton radius R_p^{point} and point-neutron radius R_n^{point} obtained with the Sky3D [38] and DIRHB [39] codes with different nuclear interactions.

Interaction	R_p^{point}	R_n^{point}
Sky3D		
SkI3 [40]	3.33	3.43
SkI4 [40]	3.31	3.41
Sly4 [41]	3.38	3.46
Sly5 [41]	3.37	3.45
Sly6 [41]	3.36	3.44
Sly4d [42]	3.35	3.44
SV-bas [43]	3.33	3.42
UNEDF0 [44]	3.37	3.47
UNEDF1 [45]	3.33	3.43
SkM* [46]	3.37	3.45
SkP [47]	3.40	3.48
DIRHB		
DD-ME2 [48]	3.30	3.39
DD-PC1 [49]	3.30	3.39

$$R_n^2 = (R_n^{\mathrm{point}})^2 + \langle r_n^2\rangle, \tag{19}$$

where $\langle r_n^2\rangle^{1/2} \simeq \langle r_p^2\rangle^{1/2}$ is the radius of the neutron (this approximation is supported by the measured value of the neutron magnetic radius $\langle r_n^2\rangle_{\mathrm{mag}}^{1/2} = 0.864^{+0.009}_{-0.008}$ fm [21] that is close to the measured value of the proton charge radius $\langle r_p^2\rangle^{1/2} = 0.8414 \pm 0.0019$ fm [36]). Hence, from the nuclear model prediction $R_n^{\mathrm{point}} \simeq R_p^{\mathrm{point}} + 0.1$ fm we obtain the approximate relation

$$R_n \simeq R_p + 0.1 \text{ fm}. \tag{20}$$

Therefore, in our analyses of the COHERENT argon data we consider two cases:

[1]Other contributions considered in Refs. [34,35] are negligible. They are the Darwin-Foldy contribution $3/4M^2 \simeq 0.033$ fm^2 and the spin-orbit charge density contribution $\langle r^2\rangle_{\mathrm{so}} \simeq 0.002$ fm^2.

Fixed R_n where R_n is given by Eq. (20) with the value in Eq. (18) for R_p:

$$R_n = 3.55 \text{ fm}. \tag{21}$$

Free R_n where R_n is considered as a free parameter between R_p and 4 fm:

$$3.45 < R_n < 4 \text{ fm}. \tag{22}$$

The CEνNS event rate in the COHERENT experiment [13] depends on the neutrino flux dN_ν/dE produced from the Spallation Neutron Source (SNS) at Oak Ridge Spallation Neutron Source. It is given by the sum of

$$\frac{dN_{\nu_\mu}}{dE} = \eta\delta\left(E - \frac{m_\pi^2 - m_\mu^2}{2m_\pi}\right), \tag{23}$$

$$\frac{dN_{\nu_{\bar{\mu}}}}{dE} = \eta\frac{64E^2}{m_\mu^3}\left(\frac{3}{4} - \frac{E}{m_\mu}\right), \tag{24}$$

$$\frac{dN_{\nu_e}}{dE} = \eta\frac{192E^2}{m_\mu^3}\left(\frac{1}{2} - \frac{E}{m_\mu}\right), \tag{25}$$

with the normalization factor $\eta = rN_{\text{POT}}/4\pi L^2$, where $r = (9 \pm 0.9) \times 10^{-2}$ is the number of neutrinos per flavor that are produced for each proton-on-target (POT), $N_{\text{POT}} = 13.7 \times 10^{22}$ is the number of protons on target corresponding to a total integrated beam power of 6.12 GW hr, and $L = 27.5$ m is the distance between the source and the COHERENT Ar detector, called CENNS-10 [1]. The pions decay at rest ($\pi^+ \to \mu^+ + \nu_\mu$) producing ν_μ's which arrive at the COHERENT detector as a prompt signal within about 1.5 μs after protons on target. The decay at rest of μ^+ ($\mu^+ \to e^+ + \nu_e + \bar{\nu}_\mu$) produces a delayed component of $\bar{\nu}_\mu$'s and ν_e's, since they arrive at the detector in a relatively longer time interval of about 10 μs. In order to extract the physical parameter of interest, the first step is to simulate the CEνNS signal at CENNS-10 as a function of the nuclear recoil energy. The theoretical CEνNS event number $N_i^{\text{CE}\nu\text{NS}}$ in each nuclear recoil energy bin i is given by

$$N_i^{\text{CE}\nu\text{NS}} = N(\text{Ar}) \int_{T_{\text{nr}}^i}^{T_{\text{nr}}^{i+1}} dT_{\text{nr}} A(T_{\text{nr}}) \int_{E_{\text{min}}}^{E_{\text{max}}} dE \times \sum_{\nu=\nu_e,\nu_\mu,\bar{\nu}_\mu} \frac{dN_\nu}{dE}\frac{d\sigma_{\nu-\mathcal{N}}}{dT_{\text{nr}}}(E, T_{\text{nr}}), \tag{26}$$

where $A(T_{\text{nr}})$ is the energy-dependent reconstruction efficiency given in Fig. 3 in Ref. [13], $E_{\text{min}} = \sqrt{MT_{\text{nr}}/2}$ and $E_{\text{max}} = m_\mu/2 \sim 52.8$ MeV, m_μ being the muon mass, $N(\text{Ar})$ is the number of Ar atoms in the detector, and $\frac{dN_\nu}{dE}$ is the neutrino flux integrated over the experiment lifetime. Concerning the former element, we digitalize the efficiency as a function of the electron-equivalent recoil energy $T_{ee}[\text{keV}_{ee}]$, which is subsequently transformed as a function of the nuclear recoil energy $T_{\text{nr}}[\text{keV}_{\text{nr}}]$ thanks to the relation

$$T_{ee} = f_Q(T_{\text{nr}})T_{\text{nr}}. \tag{27}$$

Here, f_Q is the quenching factor, which is the ratio between the scintillation light emitted in nuclear and electron recoils and determines the relation between the number of detected photoelectrons and the nuclear recoil kinetic energy. Following Ref. [13], the quenching factor is parametrized as $f_Q(T_{\text{nr}}) = (0.246 \pm 0.006 \text{ keV}_{\text{nr}}) + ((7.8 \pm 0.9) \times 10^{-4})T_{\text{nr}}$ up to 125 keV_{nr}, and kept constant for larger values. The value of $N(\text{Ar})$ is given by $N_A M_{\text{det}}/M_{\text{Ar}}$, where N_A is the Avogadro number, M_{det} is the detector active mass equal to 24 kg, and $M_{\text{Ar}} = 39.96$ g/mol is the molar mass of ^{40}Ar. Actually, one should consider that atmospheric argon is contaminated by a small percentage of ^{36}Ar and ^{38}Ar, namely $F(^{36}\text{Ar}) = 0.334\%$ and $F(^{38}\text{Ar}) = 0.063\%$. However, since the amount of ^{36}Ar and ^{38}Ar is very small and the uncertainties are large, in practice one gets the same results considering $F(^{40}\text{Ar}) = 100\%$ and $F(^{36}\text{Ar}) = F(^{38}\text{Ar}) = 0$.

In Ref. [13] two independent analyses, labeled A and B, are described that differ mainly for the selection and the treatment of the background. In the following, we will use the data coming from the analysis A, whose range of interest of the nuclear recoil energy is [0, 120] keV_{ee} (corresponding to roughly [0, 350] keV_{nr}), with 12 energy bins of size equal to 10 keV_{ee}. We have also performed the analyses of the data corresponding to analysis B of the COHERENT Collaboration [13] described in the Appendix, where we considered only the determination of the radius of the nuclear neutron distribution and of the weak mixing angle.

In our analysis corresponding to analysis A of the COHERENT Collaboration [13], we considered the least-squares function

$$\chi^2_{\text{S}} = \sum_{i=1}^{12}\left(\frac{N_i^{\text{exp}} - \eta_{\text{CE}\nu\text{NS}}N_i^{\text{CE}\nu\text{NS}} - \eta_{\text{PBRN}}B_i^{\text{PBRN}} - \eta_{\text{LBRN}}B_i^{\text{LBRN}}}{\sigma_i}\right)^2 + \left(\frac{\eta_{\text{CE}\nu\text{NS}} - 1}{\sigma_{\text{CE}\nu\text{NS}}}\right)^2 + \left(\frac{\eta_{\text{PBRN}} - 1}{\sigma_{\text{PBRN}}}\right)^2 + \left(\frac{\eta_{\text{LBRN}} - 1}{\sigma_{\text{LBRN}}}\right)^2, \tag{28}$$

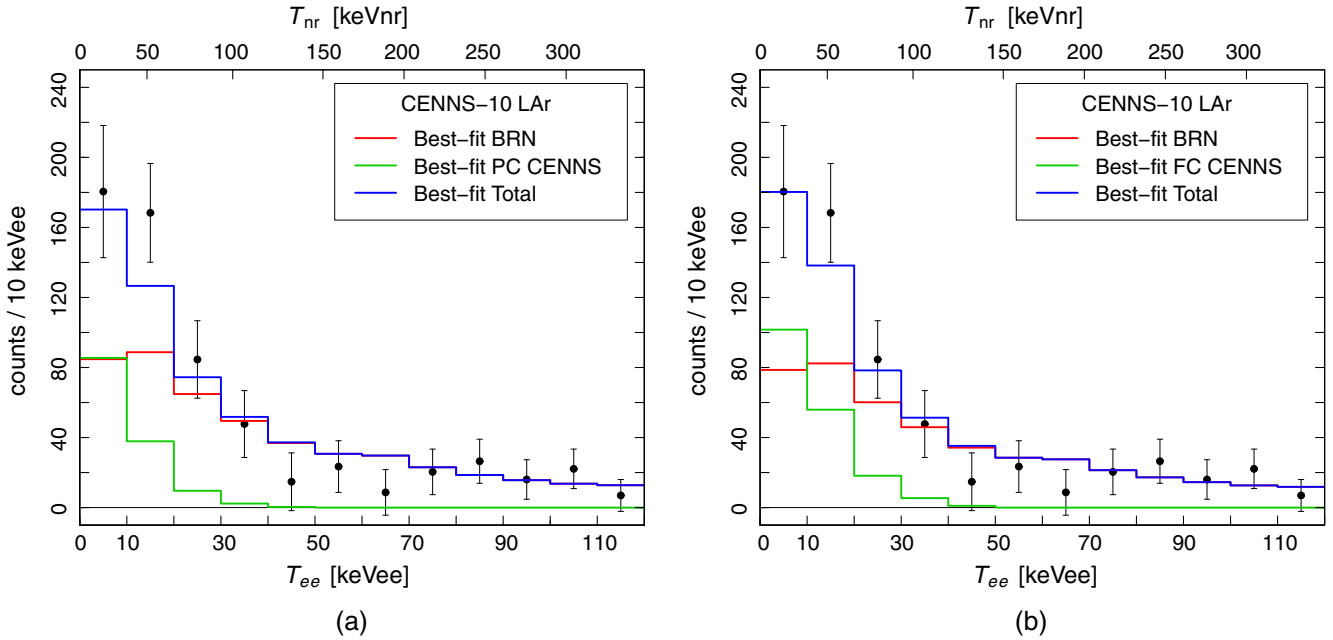

FIG. 1. Histograms representing the fits of the CENNS-10 data (black points with statistical error bars) in the case of (a) partial coherence (PC), with the neutron form factor corresponding to the minimal neutron distribution radius $R_n = 3.45$ fm, and (b) full coherence (FC).

where PBRN stands for prompt beam-related background, LBRN stands for late beam-related neutron background, and

$$\sigma_i^2 = (\sigma_i^{\rm exp})^2 + [\sigma_{\rm BRNES}(B_i^{\rm PBRN} + B_i^{\rm LBRN})]^2, \quad (29)$$

$$\sigma_{\rm BRNES} = \sqrt{\frac{0.058^2}{12}} = 1.7\%, \quad (30)$$

$$\sigma_{\rm CE\nu NS} = 13.4\% \text{ for fixed } R_n, \text{ or } 13.2\% \text{ for free } R_n, \quad (31)$$

$$\sigma_{\rm PBRN} = 32\%, \quad (32)$$

$$\sigma_{\rm LBRN} = 100\%. \quad (33)$$

For each energy bin i, $N_i^{\rm exp}$ is the experimental event number, $N_i^{\rm CE\nu NS}$ is the theoretical event number that is calculated as explained in Sec. II, $B_i^{\rm PBRN}$ and $B_i^{\rm LBRN}$ are the estimated number of PBRN and LBRN background events, and σ_i is the total signal uncertainty. The beam-related neutron energy shape (BRNES) 5.8% uncertainty ($\sigma_{\rm BRNES}$) is taken into account by distributing it over the 12 bins in an uncorrelated way. All the numbers are taken from Ref. [13].

In Eq. (29), $\eta_{\rm CE\nu NS}$, $\eta_{\rm PBRN}$, and $\eta_{\rm LBRN}$ are nuisance parameters which quantify, respectively, the systematic uncertainty of the signal rate and the systematic uncertainty of the PBRN and LBRN background rates, with corresponding standard deviations $\sigma_{\rm CE\nu NS}$, $\sigma_{\rm PBRN}$, and $\sigma_{\rm LBRN}$.

The COHERENT spectral data are shown in Fig. 1(a) together with the best-fit histogram obtained with the CEνNS cross section of Eq. (1) and the neutron form factor corresponding to the minimal neutron distribution radius $R_n = 3.45$ fm that gives the larger CEνNS cross section for R_n in the range in Eq. (22). We obtained $(\chi^2_{\rm S})_{\rm min} = 8.8$ with 11 degrees of freedom, corresponding to an excellent 64% goodness of fit. We tested also the case of full coherence, i.e., without the suppression of the neutron and proton form factors, as done in the case of the COHERENT CsI data [3,15]. In this case, illustrated in Fig. 1(b), the larger CEνNS cross section fits the low-energy data slightly better, and the medium- and high-energy data are fitted slightly better with a smaller background within the uncertainties. Indeed, the full coherence $(\chi^2_{\rm S})_{\rm min}$ is 7.0, which is smaller than the 8.8 obtained with the minimal neutron distribution radius. However, we will not consider the full coherence in the rest of the paper, because we are not aware of any physical mechanism that can justify the absence of the form-factor suppression corresponding to the physical nucleon distributions in the nucleus.

III. RADIUS OF THE NUCLEAR NEUTRON DISTRIBUTION

The observation of CEνNS scattering in argon can be used to probe the nuclear neutron distribution [3,4,16,19,50]. We fitted the COHERENT data in order to determine the neutron rms radius R_n of Ar, considering for R_n the lower bound in Eq. (22), without an upper bound.

Figure 2 shows the comparison of $\Delta\chi^2 = \chi^2_{\rm S} - (\chi^2_{\rm S})_{\rm min}$ as a function of the rms neutron distribution radius R_n of ^{40}Ar using the three most popular form factor parametrizations:

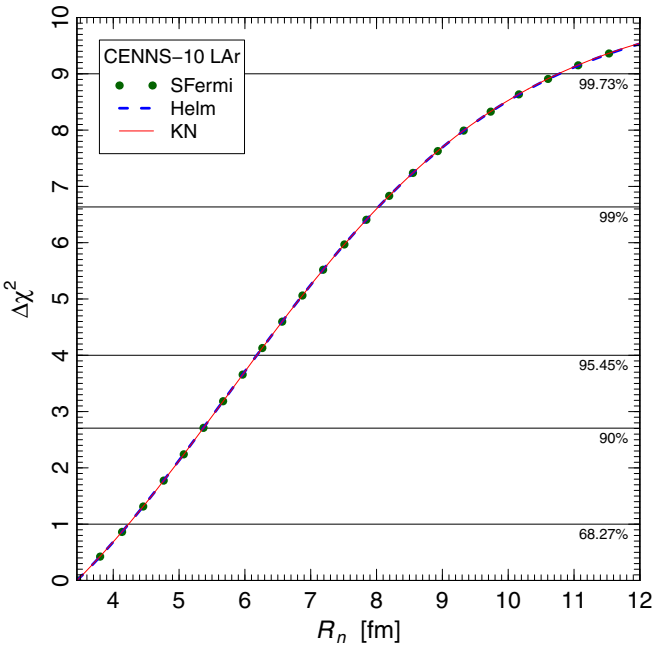

FIG. 2. $\Delta\chi^2 = \chi^2_S - (\chi^2_S)_{\min}$ as a function of the rms neutron distribution radius R_n of ^{40}Ar obtained from the fit of the data of the CENNS-10 experiment. The three curves correspond to the symmetrized Fermi [26] (SFermi), Helm [27] (Helm), and Klein-Nystrand [28] (KN) form factor parametrizations.

symmetrized Fermi [26], Helm [27], and Klein-Nystrand [28]. One can see that the three form factor parametrizations give practically the same result and the best fit is obtained for the minimal allowed value $R_n = 3.45$ fm. Therefore, from the analysis of the COHERENT data we can only put the following upper bounds on the value of the ^{40}Ar neutron distribution radius:

$$R_n(^{40}\mathrm{Ar}) < 4.2(1\sigma), 6.2(2\sigma), 10.8(3\sigma)\ \mathrm{fm}. \quad (34)$$

These bounds are in agreement with the nuclear model predictions in Table I, but unfortunately they are too weak to allow us a selection of the models.

IV. WEAK MIXING ANGLE

The weak mixing angle is a fundamental parameter in the theory of the EW interactions, and its experimental determination provides a direct probe of physics phenomena not included in the SM, usually referred to as new physics. In particular, low-energy determinations of ϑ_W offer a unique role, complementary to those at high-energy, being highly sensitive to extra Z (Z') bosons predicted in grand unified theories, technicolor models, supersymmetry, and string theories [51]. This underscores the need for improved experimental determinations of ϑ_W in the low-energy regime. We fitted the COHERENT CENNS-10 data in order to determine the value of $\sin^2\vartheta_W$ in Ar, considering R_n either fixed or free. The result for the weak mixing angle is independent on the assumption used for R_n, and in both cases we get

$$\sin^2\vartheta_W(\mathrm{Ar}) = 0.31 \pm 0.06(1\sigma), {}^{+0.11}_{-0.13}\,(2\sigma), {}^{+0.18}_{-0.23}\,(3\sigma), \quad (35)$$

which is about 1.2σ above the SM prediction, $\sin^2\vartheta_W^{\mathrm{SM}} = 0.23857(5)$ [21]. The reason of this small discrepancy is that a larger weak mixing angle increases the CEνNS cross section and it allows a better fit of the low-energy bins of the Ar data. Given the independence of $\sin^2\vartheta_W$ on the value of R_n, in the following we will consider only the case with R_n fixed. Figure 3 shows the comparison of $\Delta\chi^2 = \chi^2_S - (\chi^2_S)_{\min}$ as a function of $\sin^2\vartheta_W$ using the Helm parametrization for the neutron form factor.

Following the approach used in Ref. [15], where we improved the bounds on several physical quantities from the analysis of the COHERENT CsI data [1] considering the improved quenching factor in Ref. [52], we derive here the result for the weak mixing angle also exploiting the COHERENT CsI dataset. Fixing R_n(Cs) and R_n(I) to 5.01 fm and 4.94 fm [53], respectively, we get

$$\sin^2\vartheta_W(\mathrm{CsI}) = 0.24 \pm 0.04(1\sigma), \pm 0.09(2\sigma), {}^{+0.13}_{-0.14}\,(3\sigma), \quad (36)$$

in very good agreement with the SM prediction. The corresponding $\Delta\chi^2$ is also shown in Fig. 3. Finally, we performed a combined fit of the CsI and Ar data. The value found for the weak mixing angle is

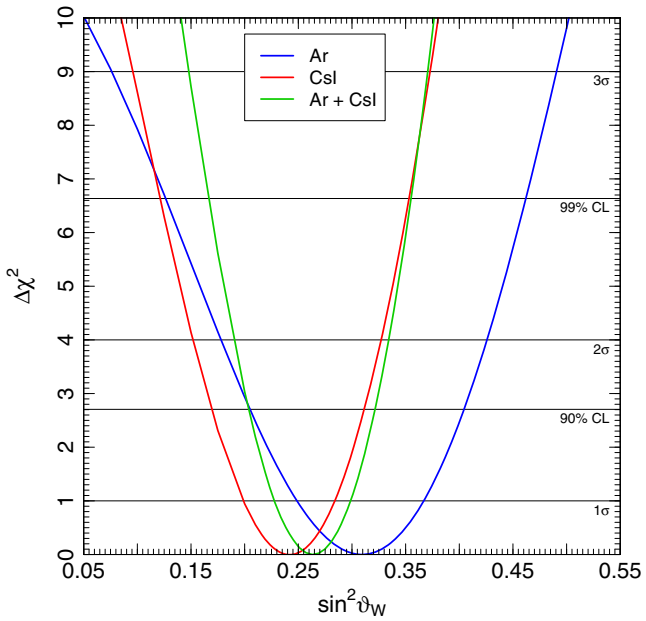

FIG. 3. $\Delta\chi^2 = \chi^2_S - (\chi^2_S)_{\min}$ as a function $\sin^2\vartheta_W$ obtained (blue line) from the fit of the data of the Ar CENNS-10 experiment, (red line) from the fit of the COHERENT CsI data, and (green line) from the combined fit.

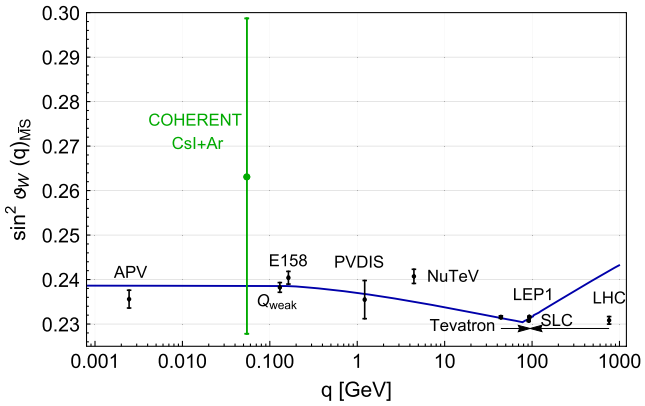

FIG. 4. Variation of $\sin^2\vartheta_W$ with energy scale q. The SM prediction is shown as the solid curve, together with experimental determinations in black at the Z pole [21] (Tevatron, LEP1, SLC, LHC), from APV on cesium [54,55], which has a typical momentum transfer given by $\langle q\rangle \simeq 2.4$ MeV, Møller scattering [56] (E158), deep inelastic scattering of polarized electrons on deuterons [57] (e^2H PVDIS), as well as from neutrino-nucleus scattering [58] (NuTeV) and the new result from the proton's weak charge at $q = 0.158$ GeV [59] (Q_{weak}). In green the result derived in this paper is shown, obtained fitting the Ar and CsI COHERENT dataset. For clarity we displayed the Tevatron and LHC points horizontally to the left and to the right, respectively.

$$\sin^2\vartheta_W(\mathrm{CsI}+\mathrm{Ar}) = 0.26^{+0.04}_{-0.03}(1\sigma), \pm 0.07(2\sigma), \pm 0.11(3\sigma), \tag{37}$$

which is slightly more precise than the CsI result alone and in agreement within 1σ with the SM prediction. Unfortunately, as it is possible to see in Fig. 4, the uncertainty obtained for the weak mixing angle from COHERENT is still very large when compared to the other determinations at low-momentum transfer.

For the proton coupling coefficient g_V^p, we obtain

$$\begin{aligned} g_V^p(\nu_e;\mathrm{CsI}+\mathrm{Ar}) &= -0.003^{+0.060}_{-0.080} \quad \text{and} \\ g_V^p(\nu_\mu;\mathrm{CsI}+\mathrm{Ar}) &= -0.011^{+0.060}_{-0.080}. \end{aligned} \tag{38}$$

These values differ from the SM predictions in Eqs. (10) and (11) by less than 1σ and confirm that the proton coupling is much smaller than the neutron coupling in the CEνNS process.

V. NEUTRINO CHARGE RADII

The neutrino charge radii are the only electromagnetic properties of neutrinos that are nonzero in the Standard Model of electroweak interactions. They are induced by radiative corrections, with the predicted values [23–25]

$$\langle r^2_{\nu_\ell}\rangle_{\mathrm{SM}} = -\frac{G_F}{2\sqrt{2}\pi^2}\left[3 - 2\ln\left(\frac{m_\ell^2}{m_W^2}\right)\right], \tag{39}$$

where m_W and m_ℓ are the W boson and charged lepton masses ($\ell = e,\ \mu,\ \tau$), and we use the conventions in Refs. [10,15,60]. The Standard Model charge radii of neutrinos are diagonal in the flavor basis, because in the Standard Model the generation lepton numbers are conserved. Numerically, the predicted values of $\langle r^2_{\nu_e}\rangle_{\mathrm{SM}}$ and $\langle r^2_{\nu_\mu}\rangle_{\mathrm{SM}}$ that can be probed with the data of the COHERENT experiment are

$$\langle r^2_{\nu_e}\rangle_{\mathrm{SM}} = -0.83\times 10^{-32}\ \mathrm{cm}^2, \tag{40}$$

$$\langle r^2_{\nu_\mu}\rangle_{\mathrm{SM}} = -0.48\times 10^{-32}\ \mathrm{cm}^2. \tag{41}$$

The current 90% C.L. experimental bounds for $\langle r^2_{\nu_e}\rangle$ and $\langle r^2_{\nu_\mu}\rangle$ obtained in laboratory experiments that do not involve CEνNS are listed in Table I of Ref. [10]. Since they are only about 1 order of magnitude larger than the Standard Model predictions, they may be the first neutrino electromagnetic properties measured by new experiments in the near future.

As discussed in Sec. II the contribution of the Standard Model charge radius of ν_ℓ is taken into account by the last term in the expression (3) of $g_V^p(\nu_\ell)$. Here, we want to study the effects of the neutrino charge radii in the CEνNS data of the COHERENT experiment independently of the origin of the charge radii that can have contributions both from the Standard Model and from physics beyond the Standard Model. Therefore we consider the differential cross section

$$\frac{d\sigma_{\nu_\ell-\mathcal{N}}}{dT_{\mathrm{nr}}}(E,T_{\mathrm{nr}}) = \frac{G_F^2 M}{\pi}\left(1-\frac{MT_{\mathrm{nr}}}{2E^2}\right)\left\{[(\tilde{g}_V^p - \tilde{Q}_{\ell\ell})ZF_Z(|\vec{q}|^2) + g_V^n NF_N(|\vec{q}|^2)]^2 + Z^2F_Z^2(|\vec{q}|^2)\sum_{\ell'\neq\ell}|\tilde{Q}_{\ell'\ell}|^2\right\}, \tag{42}$$

where $\tilde{g}_V^p = 0.0204$ is given by Eq. (3) without the last term that contains the contribution of the Standard Model charge radius. The effects of the charge radii $\langle r^2_{\nu_{\ell\ell'}}\rangle$ in the cross section are expressed through [61]

$$\tilde{Q}_{\ell\ell'} = \frac{\sqrt{2}\pi\alpha}{3G_F}\langle r^2_{\nu_{\ell\ell'}}\rangle. \tag{43}$$

We consider the general case in which neutrinos can have both diagonal and off-diagonal charge radii in the flavor basis. The off-diagonal charge radii, as well as part of the diagonal charge radii, can be generated by physics beyond the Standard Model.

The effects of the charge radii in the cross section are sometimes expressed through [62,63]

$$\hat{Q}_{\ell\ell'} = \frac{2}{3} m_W^2 \sin^2\vartheta_W \langle r^2_{\nu_{\ell\ell'}}\rangle, \tag{44}$$

which is considered equivalent to $\tilde{Q}_{\ell\ell'}$ in Eq. (43) [64] through the well-known relations $G_F/\sqrt{2} = g^2/8m_W^2$ and $g^2\sin^2\vartheta_W = e^2 = 4\pi\alpha$, where g is the weak charged-current coupling constant and e is the elementary electric charge (see, for example, Ref. [65]). The problem is that the equivalence holds only at tree level and radiative corrections induce a significant difference. Indeed, using the PDG values of all quantities [21] we obtain, neglecting the uncertainties, $\sqrt{2}\pi\alpha/3G_F = 2.38\times10^{30}$ cm^{-2} and $2m_W^2\sin^2\vartheta_W/3 = 2.64\times10^{30}$ cm^{-2}, that differ by about 10%. Therefore, the form in Eq. (44) overestimates the effect of the charge radius by about 10% with respect to the form in Eq. (43) that is the correct one for low-energy interactions because it depends only on measured low-energy quantities. Moreover, one can notice that the electromagnetic interaction due to the charge radius must be proportional to the electromagnetic fine-structure constant α and must be independent of the Fermi weak interaction constant G_F. Indeed, the G_F in the denominator of Eq. (43) cancels the G_F in the cross section (42).

The diagonal charge radii of flavor neutrinos contribute to the cross section coherently with the neutrino-proton neutral current interaction, generating an effective shift of $\sin^2\vartheta_W$. In the case of $\bar{\nu}_\ell - \mathcal{N}$ scattering, we have $g_V^{p,n} \to -g_V^{p,n}$ and $\langle r_{\nu_{\ell\ell'}}\rangle \to \langle r_{\bar{\nu}_{\ell\ell'}}\rangle = -\langle r_{\nu_{\ell\ell'}}\rangle$. Therefore, the charge radii of flavor neutrinos and antineutrinos contribute with the same sign to the shift of $\sin^2\vartheta_W$ in the CEνNS cross section.

There are five charge radii that can be determined with the COHERENT CEνNS data: the two diagonal charge radii $\langle r^2_{\nu_{ee}}\rangle$ and $\langle r^2_{\nu_{\mu\mu}}\rangle$ that sometimes are denoted with the simpler notation $\langle r^2_{\nu_e}\rangle$ and $\langle r^2_{\nu_\mu}\rangle$ in connection to the Standard Model charge radii in Eqs. (39)–(41), and the absolute values of the three off-diagonal charge radii $\langle r^2_{\nu_{e\mu}}\rangle = \langle r^2_{\nu_{\mu e}}\rangle^*$, $\langle r^2_{\nu_{e\tau}}\rangle$, and $\langle r^2_{\nu_{\mu\tau}}\rangle$.

In Ref. [10] we obtained the bounds on the neutrino charge radii from the analysis of the COHERENT CsI data [1]. In Ref. [15] we improved these bounds considering the improved quenching factor in Ref. [52]. Here we present the bounds on the neutrino charge radii that we obtained from the analysis of the spectral Ar data of the COHERENT experiment [13] and those obtained with a combined fit of the CsI and Ar data. We also revise the CsI limits on the charge radii presented in Ref. [15] because they have been obtained through Eq. (44), which overestimates their contribution by about 10%, as discussed above.

The results of our fits for fixed and free R_n are given in Table II. One can see that the bounds obtained with fixed and free R_n are similar. Therefore, our results are practically independent from the unknown value of R_n, and in the following, for simplicity, we discuss only the case of fixed R_n.

TABLE II. Limits at 1σ, 2σ, and 3σ for the neutrino charge radii in units of 10^{-32} cm^2, obtained from the analysis of the COHERENT CsI and Ar data, and from the combined fit.

	Fixed R_n			Free R_n		
	1σ	2σ	3σ	1σ	2σ	3σ
			CsI			
$\langle r^2_{\nu_{ee}}\rangle$	$-55 \div -2$	$-67 \div 11$	$-76 \div 20$	$-54 \div 1$	$-66 \div 14$	$-76 \div 24$
$\langle r^2_{\nu_{\mu\mu}}\rangle$	$-64 \div 8$	$-68 \div 12$	$-73 \div 17$	$-64 \div 10$	$-68 \div 15$	$-72 \div 20$
$\langle r^2_{\nu_{e\mu}}\rangle$	<26	<32	<37	<26	<32	<36
$\langle r^2_{\nu_{e\tau}}\rangle$	<27	<39	<48	<27	<39	<48
$\langle r^2_{\nu_{\mu\tau}}\rangle$	<36	<40	<45	<36	<40	<45
			Ar			
$\langle r^2_{\nu_{ee}}\rangle$	$-89 \div 39$	$-98 \div 48$	$-108 \div 58$	$-89 \div 38$	$-97 \div 47$	$-107 \div 57$
$\langle r^2_{\nu_{\mu\mu}}\rangle$	$-63 \div 12$	$-73 \div 22$	$-80 \div 30$	$-63 \div 9$	$-72 \div 22$	$-80 \div 29$
$\langle r^2_{\nu_{e\mu}}\rangle$	<34	<40	<46	<33	<40	<46
$\langle r^2_{\nu_{e\tau}}\rangle$	<64	<73	<83	<63	<72	<82
$\langle r^2_{\nu_{\mu\tau}}\rangle$	<37	<48	<55	<36	<47	<54
			CsI + Ar			
$\langle r^2_{\nu_{ee}}\rangle$	$-56 \div -2$	$-68 \div 11$	$-78 \div 22$	$-55 \div -4$	$-67 \div 14$	$-77 \div 25$
$\langle r^2_{\nu_{\mu\mu}}\rangle$	$-64 \div 6$	$-68 \div 12$	$-71 \div 17$	$-64 \div 9$	$-67 \div 15$	$-71 \div 19$
$\langle r^2_{\nu_{e\mu}}\rangle$	<27	<33	<36	<25	<32	<36
$\langle r^2_{\nu_{e\tau}}\rangle$	<27	<40	<50	<26	<40	<50
$\langle r^2_{\nu_{\mu\tau}}\rangle$	<36	<40	<44	<36	<40	<44

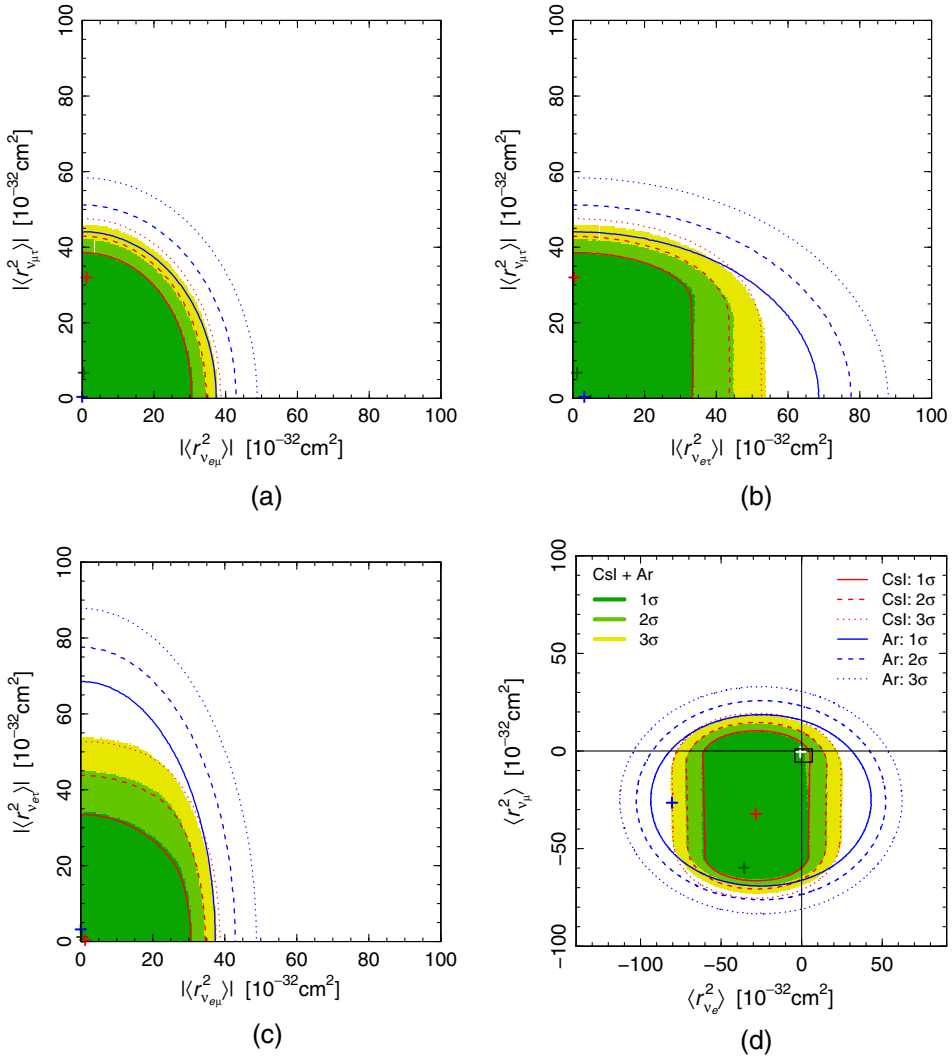

FIG. 5. Contours of the allowed regions in different planes of the neutrino charge radii parameter space obtained with fixed R_n obtained from the analysis of COHERENT CsI data (red lines), from the analysis of COHERENT Ar data in this paper (blue lines), and from the combined fit (shaded green-yellow regions). The crosses with the corresponding colors indicate the best fit points. The white cross near the origin in (d) indicates the Standard Model values in Eqs. (40) and (41). The black rectangle near the origin shows the 90% bounds on $\langle r^2_{\nu_e}\rangle$ and $\langle r^2_{\nu_\mu}\rangle$ obtained, respectively, in the TEXONO [66] and BNL-E734 [67] experiments.

The bounds in Table II obtained from the COHERENT Ar data are compatible, but less stringent than those obtained from the CsI data, and the bounds of the combined fit are similar to those obtained with the CsI data only. This is illustrated by Fig. 5, which depicts the allowed regions in different planes of the parameter space of the neutrino charge radii. It is interesting, however, that the contribution of the argon data shrinks the allowed region in the vicinity of the Standard Model values of the diagonal charge radii given in Eqs. (40) and (41) and shown by the white cross near the origin in Fig. 5(d). In the combined fit, the point corresponding to the Standard Model values of the diagonal charge radii lies at the edge of the 1σ allowed region. The best fit of the COHERENT Ar data is obtained for relatively large values of the charge radii shown by the blue crosses in Fig. 5. As shown in Fig. 6, the resulting enhancement of the CEνNS cross section with respect to the SM allows a better fit of the low-energy data, while the medium- and high-energy data are fitted better with a slightly lower background allowed by the uncertainties. The best-fit large values of $\langle r^2_{\nu_e}\rangle$ and $\langle r^2_{\nu_\mu}\rangle$ are, however, completely excluded by the bounds obtained by other experiments (see Table I of Ref. [10]). The black rectangle near the origin in Fig. 5(d) shows the most stringent 90% bounds on $\langle r^2_{\nu_e}\rangle$ and $\langle r^2_{\nu_\mu}\rangle$ obtained, respectively, in the TEXONO [66] and BNL-E734 [67] experiments. Unfortunately the CEνNS data still do not allow us to limit the neutrino charge radii with such small precision, but it is interesting to see that they tend to favor negative values of the charge radii.

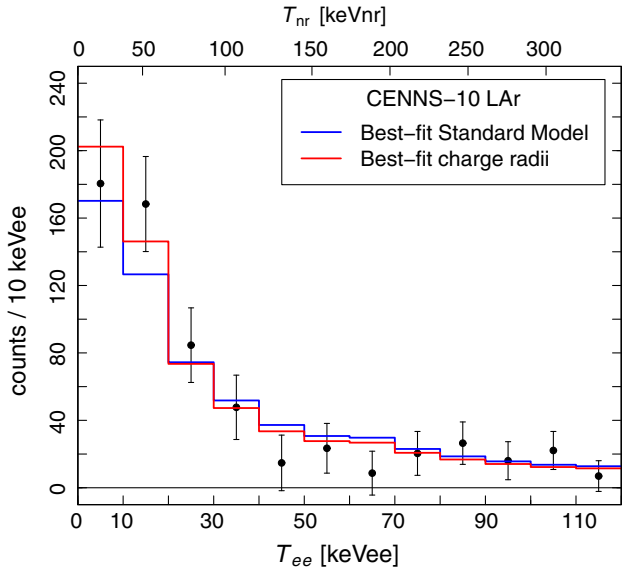

FIG. 6. Histogram representing the fits of the CENNS-10 data (black points with statistical error bars) with the Standard Model charge radii given in Eqs. (40) and (41) (blue histogram), and with the best-fit charge radii of the COHERENT Ar data analysis (red histogram).

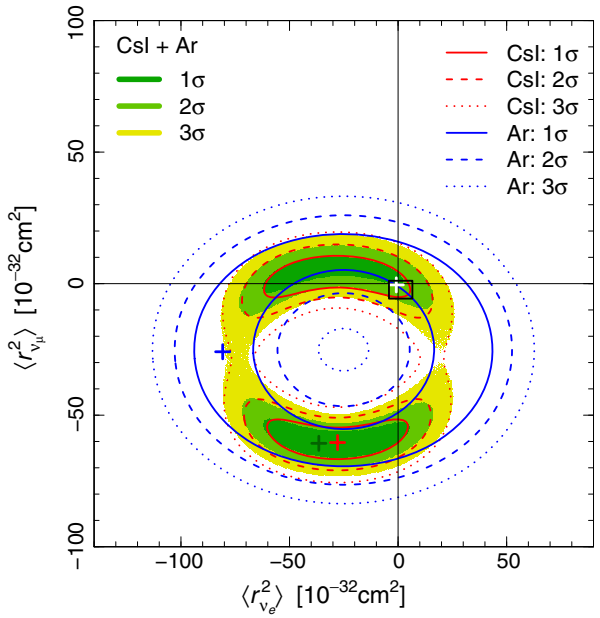

FIG. 7. Contours of the allowed regions in the $(\langle r^2_{\nu_e} \rangle, \langle r^2_{\nu_\mu} \rangle)$ plane obtained with fixed R_n obtained from the analysis of COHERENT CsI data (red lines), from the analysis of COHERENT Ar data in this paper (blue lines), and from the combined fit (shaded green-yellow regions), assuming the absence of transition charge radii. The crosses with the corresponding colors indicate the best fit points. The white cross near the origin indicates the Standard Model values in Eqs. (40) and (41). The black rectangle near the origin shows the 90% bounds on $\langle r^2_{\nu_e} \rangle$ and $\langle r^2_{\nu_\mu} \rangle$ obtained, respectively, in the TEXONO [66] and BNL-E734 [67] experiments.

We considered also the case of the absence of the neutrino transition charge radii that is motivated by the attempt to probe the values of the neutrino charge radii in the Standard Model, where only the diagonal charge radii with the values in Eqs. (40) and (41) exist. It is also possible that the physics beyond the Standard Model generates off-diagonal neutrino charge radii that are much smaller than the diagonal charge radii and can be neglected in a first approximation. Figure 7 shows the allowed regions in the $(\langle r^2_{\nu_e} \rangle, \langle r^2_{\nu_\mu} \rangle)$ plane. One can see that the contribution of the Ar data leads to a restriction of the allowed regions. Although the combined fit tends to favor the allowed island at large negative values of $\langle r^2_{\nu_\mu} \rangle$, we cannot consider it as possible, because it lies well outside the black rectangle near the origin that shows the 90% bounds of the TEXONO [66] and BNL-E734 [67] experiments. The allowed island of the combined CsI and Ar analysis for values of $\langle r^2_{\nu_\mu} \rangle$ around zero is compatible at about 2σ with these bounds, as well as with the Standard Model values of the neutrino charge radii.

VI. NEUTRINO ELECTRIC CHARGES

As discussed in Ref. [10], the CEνNS process is sensitive not only to the neutrino charge radii but also to the neutrino electric charges. Usually neutrinos are considered as exactly neutral particles, but in theories beyond the SM they can have small electric charges (often called milli-charges). This possibility was considered in many experimental and theoretical studies (see the review in Ref. [60]).

The differential CEνNS cross section that takes into account the contribution of the neutrino electric charges in addition to Standard Model neutral-current weak interactions is

$$\frac{d\sigma_{\nu_\ell-\mathcal{N}}}{dT_{\rm nr}}(E,T_{\rm nr}) = \frac{G_{\rm F}^2 M}{\pi}\left(1-\frac{MT_{\rm nr}}{2E^2}\right)\left\{[(g_V^p - Q_{\ell\ell})ZF_Z(|\vec{q}|^2) + g_V^n NF_N(|\vec{q}|^2)]^2 + Z^2F_Z^2(|\vec{q}|^2)\sum_{\ell'\neq\ell}|Q_{\ell'\ell}|^2\right\}, \quad (45)$$

with g_V^p and g_V^n given, respectively, by Eqs. (3) and (4), with the numerical values in Eqs. (10)–(12). The neutrino electric charges $q_{\nu_{\ell\ell'}}$ contribute through [60,61]

$$Q_{\ell\ell'} = \frac{2\sqrt{2}\pi\alpha}{G_F q^2} q_{\nu_{\ell\ell'}}, \tag{46}$$

where $q^2 = -2MT_{nr}$ is the squared four-momentum transfer. Although the electric charges of neutrinos and antineutrinos are opposite, neutrinos and antineutrinos contribute with the same sign to the shift of $\sin^2\vartheta_W$, as in the case of the charge radii, because also the weak neutral current couplings change sign from neutrinos to antineutrinos.

In this section, we present the bounds on the neutrino electric charges that we obtained from the analysis of the spectral Ar data of the COHERENT experiment [13] and those obtained with a combined fit of the CsI and Ar data. We also revise the CsI limits on the electric charges presented in Ref. [15] because they have been obtained through an expression similar to that in Eq. (44) [see Eq. (30) of Ref. [15]] that overestimates their contribution by about 10%, as discussed in Sec. V for the charge radii.

There are five electric charges that can be determined with the COHERENT CEνNS data: the two diagonal electric charges $q_{\nu_{ee}}$ and $q_{\nu_{\mu\mu}}$, and the absolute values of the three transition electric charges $q_{\nu_{e\mu}} = q^*_{\nu_{\mu e}}$, $q_{\nu_{e\tau}}$, and $q_{\nu_{\mu\tau}}$.

The results of our fits for fixed and free R_n are given in Table III. Since the bounds are similar in the two cases, in Fig. 8 we show only the allowed regions in different planes of the neutrino electric charge parameter space obtained with fixed R_n.

From Table III and Fig. 8 one can see that the COHERENT Ar data allow us to put slightly more stringent limits on the neutrino electric charges than the CsI data, in spite of the larger uncertainties. The larger sensitivity of the Ar data to the electric charges is in contrast with the smaller sensitivity to the charge radii discussed in Sec. V. It follows from the enhancement of the neutrino electric charge effect in CEνNS at low q^2, because of the denominator in Eq. (46). Since $q^2 = -2MT_{nr}$, light nuclei are more sensitive than heavier ones at the neutrino electric charges for similar nuclear recoil kinetic energies T_{nr}. The acceptance functions of both the CsI and Ar experiments have a threshold of about 5 keV_{nr}. Since $M(^{40}\text{Ar}) \simeq 37$ GeV, $M(^{133}\text{Cs}) \simeq 123$ GeV, and $M(^{127}\text{I}) \simeq 118$ GeV, the minimum value of $|q^2|$ can be about 3.2 times smaller in the Ar experiment than in the CsI experiment. However, this enhancement of a factor as large as 3.2 of the neutrino electric charge effect for nuclear recoil kinetic energies above the experimental threshold is mitigated by the different sizes of the energy bins: in the Ar experiment the first bin includes energies from the threshold to about 36 keV_{nr}, whereas the CsI energy bins have a size of about 1.7 keV_{nr}. Therefore, the enhancement of the electric charge effect occurs only in the first energy bin of the Ar experiment. Nevertheless, this enhancement is sufficient for achieving a slightly better performance of the Ar data in constraining the neutrino electric charges in spite of the larger uncertainties, as can be seen in Table III and Fig. 8.

The combined fit of the COHERENT CsI and Ar data leads to a significant restriction of the allowed values of the neutrino electric charges, especially the diagonal ones, because of the incomplete overlap of the CsI and Ar

TABLE III. Limits at 1σ, 2σ, and 3σ for the neutrino electric charges in units of $10^{-8}e$, obtained from the analysis of the COHERENT CsI and Ar data, and from the combined fit.

	Fixed R_n			Free R_n		
	1σ	2σ	3σ	1σ	2σ	3σ
			CsI			
$q_{\nu_{ee}}$	$0 \div 37$	$-13 \div 57$	$-24 \div 71$	$0 \div 39$	$-15 \div 57$	$-27 \div 71$
$q_{\nu_{\mu\mu}}$	$-8 \div 8$	$-13 \div 27$	$-19 \div 47$	$-8 \div 9$	$-14 \div 28$	$-20 \div 47$
$\lvert q_{\nu_{e\mu}}\rvert$	<17	<28	<35	<18	<28	<35
$\lvert q_{\nu_{e\tau}}\rvert$	<23	<38	<51	<23	<38	<51
$\lvert q_{\nu_{\mu\tau}}\rvert$	<23	<34	<41	<24	<34	<41
			Ar			
$q_{\nu_{ee}}$	$-17 \div 18$	$-23 \div 38$	$-28 \div 47$	$-16 \div 18$	$-23 \div 38$	$-28 \div 47$
$q_{\nu_{\mu\mu}}$	$-8 \div 14$	$-11 \div 28$	$-15 \div 35$	$-7 \div 14$	$-11 \div 28$	$-15 \div 35$
$\lvert q_{\nu_{e\mu}}\rvert$	<12	<18	<21	<12	<17	<21
$\lvert q_{\nu_{e\tau}}\rvert$	<22	<32	<38	<21	<32	<38
$\lvert q_{\nu_{\mu\tau}}\rvert$	<14	<21	<25	<14	<21	<25
			CsI + Ar			
$q_{\nu_{ee}}$	$-4 \div 24$	$-14 \div 34$	$-20 \div 42$	$-5 \div 23$	$-14 \div 34$	$-20 \div 41$
$q_{\nu_{\mu\mu}}$	$-7 \div 4$	$-10 \div 12$	$-12 \div 20$	$-7 \div 3$	$-10 \div 12$	$-13 \div 20$
$\lvert q_{\nu_{e\mu}}\rvert$	<11	<17	<20	<11	<16	<20
$\lvert q_{\nu_{e\tau}}\rvert$	<18	<27	<34	<17	<27	<33
$\lvert q_{\nu_{\mu\tau}}\rvert$	<14	<20	<25	<14	<20	<24

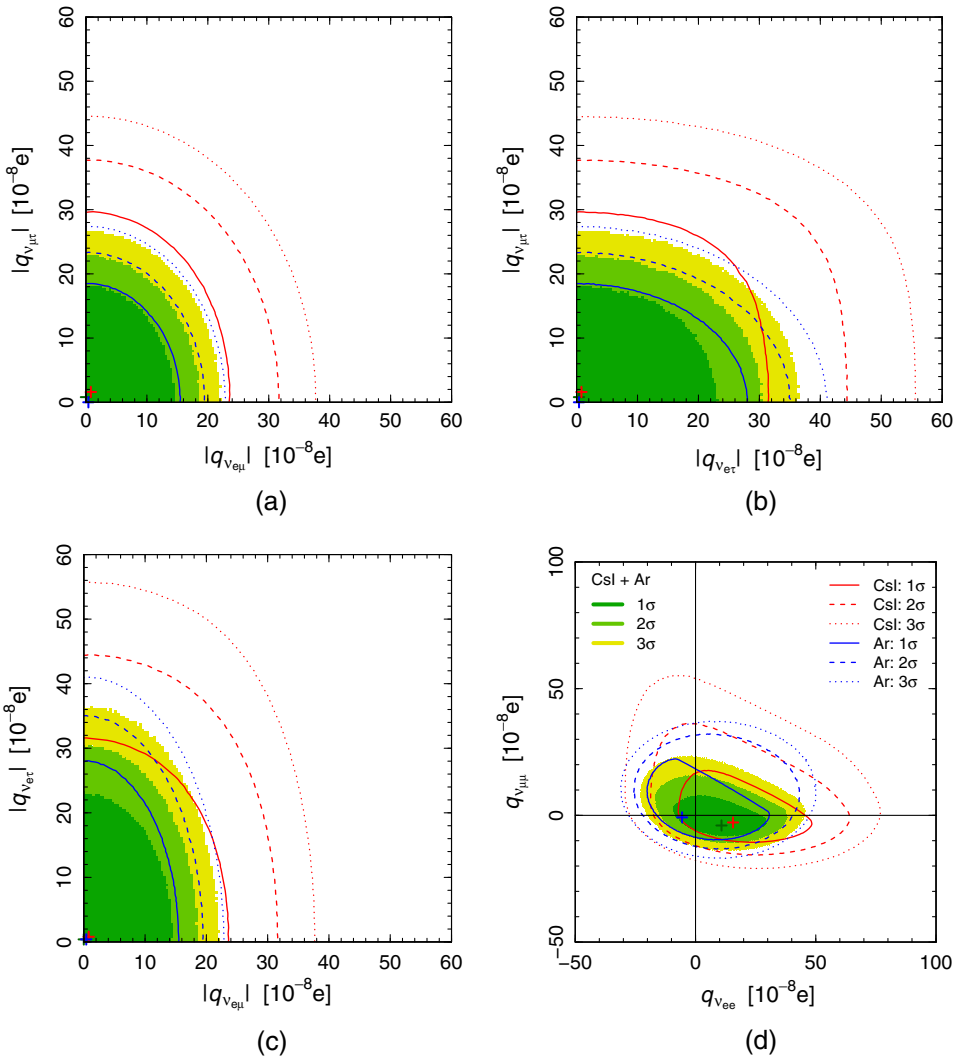

FIG. 8. Contours of the allowed regions in different planes of the neutrino electric charge parameter space obtained with fixed R_n obtained from the analysis of COHERENT CsI data (red lines), from the analysis of COHERENT Ar data in this paper (blue lines), and from the combined fit (shaded green-yellow regions). The crosses with the corresponding colors indicate the best fit points.

allowed regions that can be seen in Fig. 8(d). Although the best-fit values of $q_{\nu_{ee}}$ and $q_{\nu_{\mu\mu}}$ are visibly different from zero, the deviation is not significant, because the 1σ allowed region includes well the point $q_{\nu_{ee}} = q_{\nu_{\mu\mu}} = 0$. From Figs. 8(a), 8(b), and 8(c), one can see that the best-fit values of the off-diagonal electric charges are close to zero and the values of the off-diagonal electric charges are well constrained.

As already noted in Ref. [15], the bounds of the order of $10^{-7}e$ that we obtained are not competitive with the bounds on the electron neutrino electric charges obtained in reactor neutrino experiments that are at the level of $10^{-12}e$ [21,60,68,69]. These limits are given in the literature for the diagonal electron neutrino charge $q_{\nu_{ee}}$, because the contribution of the off-diagonal charges was not considered. However, since the off-diagonal charges contribute to the cross section in a quantitatively comparable way, we can consider them to be bounded at the same order of magnitude of $10^{-12}e$. Therefore our bounds are not competitive with the reactor bounds for $q_{\nu_{ee}}$, $q_{\nu_{e\mu}}$, and $q_{\nu_{e\tau}}$. On the other hand, they are the only existing laboratory bounds for $q_{\nu_{\mu\mu}}$ and $q_{\nu_{\mu\tau}}$.

VII. NEUTRINO MAGNETIC MOMENTS

The neutrino magnetic moment is the electromagnetic neutrino property that is most studied and searched experimentally. The reason is that its existence is predicted by many models beyond the Standard Model, especially those that include right-handed neutrinos. It is also phenomenologically important for astrophysics because neutrinos with a magnetic moment can interact with astrophysical magnetic fields leading to several important effects (see the reviews in Refs. [60,70]).

TABLE IV. Limits at 1σ, 2σ, and 3σ for the neutrino magnetic moments in units of $10^{-10}\mu_B$, obtained from the analysis of COHERENT CsI data in Ref. [15], from the analysis of COHERENT Ar data in this paper, and from the combined fit.

	Fixed R_n			Free R_n		
	1σ	2σ	3σ	1σ	2σ	3σ
			CsI			
$\lvert\mu_{\nu_e}\rvert$	<24	<42	<58	<33	<50	<65
$\lvert\mu_{\nu_\mu}\rvert$	<26	<34	<42	$3 \div 31$	<39	<46
			Ar			
$\lvert\mu_{\nu_e}\rvert$	<55	<70	<85	<55	<70	<85
$\lvert\mu_{\nu_\mu}\rvert$	<39	<50	<60	<39	<50	<60
			CsI + Ar			
$\lvert\mu_{\nu_e}\rvert$	<27	<44	<56	<33	<48	<60
$\lvert\mu_{\nu_\mu}\rvert$	$5 \div 27$	<34	<41	$12 \div 31$	<37	<43

The CEνNS process is sensitive to neutrino magnetic moments [7,15,29,30,71,72]. In this section, we present the bounds on the neutrino magnetic moments that we obtained from the analysis of the COHERENT Ar data and those that we obtained from the combined fit of the COHERENT CsI and Ar data.

For the analysis of the COHERENT data we used the least-squares function in Eq. (29), with the theoretical predictions $N_i^{\mathrm{CE}\nu\mathrm{NS}}$ calculated by adding to the Standard Model weak cross section in Eq. (1) the magnetic moment interaction cross section

$$\frac{d\sigma^{\mathrm{mag}}_{\nu_\ell-\mathcal{N}}}{dT_{\mathrm{nr}}}(E,T_{\mathrm{nr}}) = \frac{\pi\alpha^2}{m_e^2}\left(\frac{1}{T_{\mathrm{nr}}}-\frac{1}{E}\right)Z^2F_Z^2(|\vec{q}|^2)\left|\frac{\mu_{\nu_\ell}}{\mu_B}\right|^2, \quad (47)$$

where m_e is the electron neutrino mass, μ_{ν_ℓ} is the effective magnetic moment of the flavor neutrino ν_ℓ in elastic scattering (see Ref. [60]), and μ_B is the Bohr magneton.

The results of the fits for fixed and free R_n are given in Table IV. Again, one can see that the bounds are robust with respect to our lack of knowledge of the value of R_n, because the bounds are similar for fixed and free R_n. For simplicity, in Fig. 9(a) we show only the allowed regions in the $(|\mu_{\nu_e}|, |\mu_{\nu_\mu}|)$ plane obtained with fixed R_n.

From Fig. 9(a) one can see that the best fit of the Ar data is obtained for relatively large values of the neutrino magnetic moments. The reason is similar to that discussed in Sec. V for the neutrino charge radii: as illustrated in Fig. 9(b), the enhancement of the CEνNS cross section with a sizable neutrino magnetic moment contribution fits better the low-energy bins of the Ar dataset than the SM cross section, and the medium- and high-energy bins are fitted better with a slightly smaller background allowed by the uncertainties. In the combined CsI and Ar analysis we find the best fit for $|\mu_{\nu_e}| = 0$, but a best-fit value of $|\mu_{\nu_\mu}|$ that is

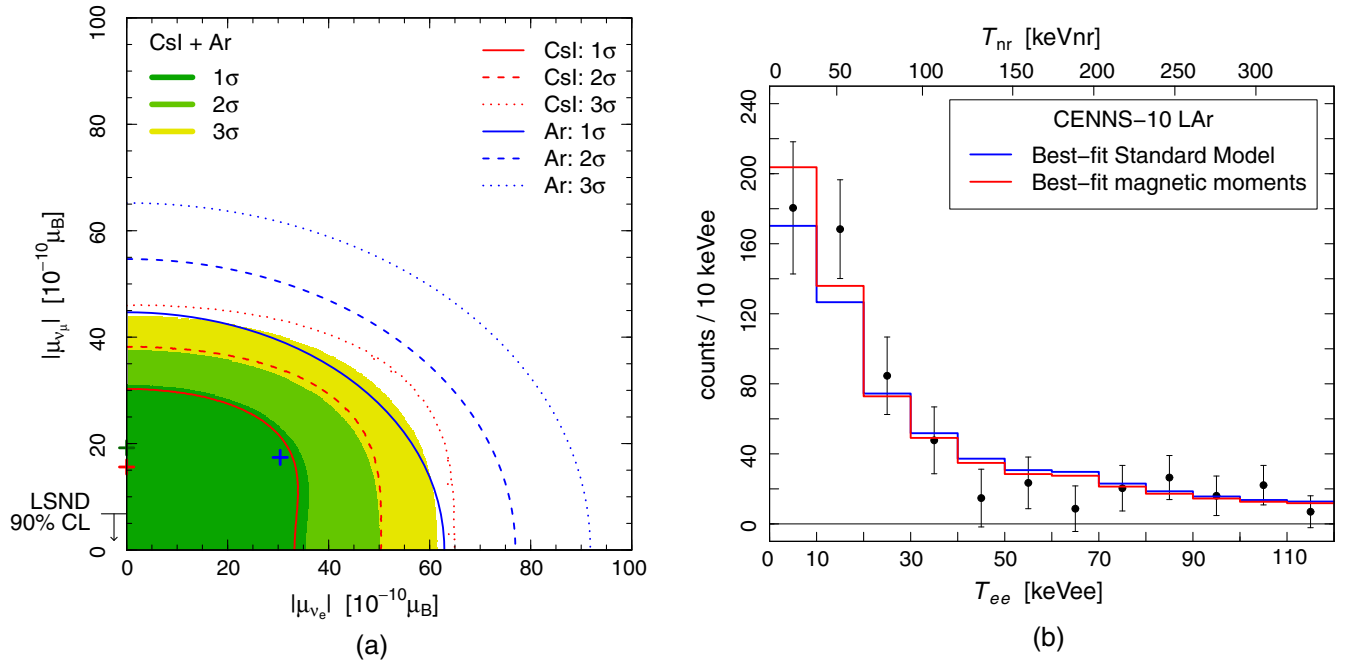

FIG. 9. (a) Contours of the allowed regions in the $(|\mu_{\nu_e}|, |\mu_{\nu_\mu}|)$ plane obtained with fixed R_n obtained from the analysis of COHERENT CsI data in Ref. [15] (red lines), from the analysis of COHERENT Ar data in this paper (blue lines), and from the combined fit (shaded green-yellow regions). The crosses with the corresponding colors indicate the best fit points. The figure shows also the LSND 90% C.L. upper bound on $|\mu_{\nu_\mu}|$ [73]. (b) Histograms representing the fits of the CENNS-10 data (black points with statistical error bars) with the Standard Model weak-interaction cross section (blue histogram), and with the best-fit magnetic moment of the COHERENT Ar data analysis (red histogram).

relatively large. However, we cannot consider this as a valid indication in favor of a nonzero $|\mu_{\nu_\mu}|$ because the best-fit value is much larger than the bounds obtained in accelerator experiments with $\nu_\mu - e$ scattering (see Table IV of Ref. [60]). The most stringent of those bounds is the LSND bound $|\mu_{\nu_\mu}| < 6.8 \times 10^{-10}\mu_B$ at 90% C.L. [73] shown in Fig. 9(a). Nevertheless, the 1σ allowed region of the combined fit is compatible with this bound, as well as with the stringent bounds on $|\mu_{\nu_e}|$ established in reactor neutrino experiments [the currently best one, $|\mu_{\nu_e}| < 2.9 \times 10^{-11}\mu_B$ [21,60,74], is not shown in Fig. 9(a) because it would not be distinguishable from the y axis].

VIII. CONCLUSIONS

In this paper we discussed the information on nuclear physics, on the low-energy electroweak mixing angle, and on the electromagnetic properties of neutrinos that can be obtained from the analysis of the recent CEνNS data on argon of the COHERENT experiment [13]. We also presented the results obtained by combining the analysis of the COHERENT Ar data with the analysis of the COHERENT CsI data [1] performed in Ref. [15].

The information on nuclear physics provided by CEνNS measurements concerns the radius of the neutron distribution in the target nucleus. In Sec. III we calculated the bounds on the radius of the neutron distribution in ^{40}Ar. These bounds are in agreement with the nuclear model predictions in Table I but are rather weak because the data have large uncertainties. Therefore, they do not allow us to discriminate the different nuclear models.

For the low-energy weak mixing angle, from the analysis of the COHERENT Ar data we obtained a relatively large value which, however, is compatible with that predicted by the Standard Model at about 1.7σ. Including in the analysis the COHERENT CsI data, we found a value that is still larger than that predicted by the Standard Model, but compatible at about 1σ.

The analysis of the COHERENT Ar data allows us to constrain the neutrino charge radii and magnetic moments, but not as well as the analysis of the COHERENT CsI data. Therefore, the combined fits are dominated by the CsI data, with small changes due to the Ar data with respect to the results obtained in Ref. [15]. On the other hand, the Ar data are more sensitive to the neutrino electric charges than the CsI data because of the lower nuclear mass, as discussed in Sec. VI. Therefore, the Ar data allowed us to improve the constraints on the neutrino electric charges that can be obtained with CEνNS. In particular, we improved the only existing laboratory bounds on the electric charge $q_{\mu\mu}$ of the muon neutrino and on the transition electric charge $q_{\mu\tau}$.

In conclusion, we would like to emphasize the importance of the results of the COHERENT experiment that opened the way for CEνNS measurements, first with the CsI detector [1] and then with the LAr detector [13]. Even if the first CEνNS data on argon have large uncertainties, they give us useful physical information. We believe that future experimental improvements will lead to far-reaching results.

ACKNOWLEDGMENTS

The work of C. G. was partially supported by the research grant "The Dark Universe: A Synergic Multimessenger Approach" No. 2017X7X85K under the program PRIN 2017 funded by the Ministero dell'Istruzione, Università e della Ricerca (MIUR). The work of Y. F. L. and Y. Y. Z. is supported by the National Natural Science Foundation of China under Grant No. 11835013. Y. F. L. is also grateful for the support by the CAS Center for Excellence in Particle Physics (CCEPP).

APPENDIX: RESULTS OBTAINED WITH THE ANALYSIS B

In Secs. III and IV, the radius of the nuclear neutron distribution and the electroweak mixing angle have been studied using the so-called analysis A of CENNS-10 data [13], whose selection criteria allow one to put more stringent constraints on the parameters of interest. For completeness, here we present the results obtained using the same fitting procedure developed in Secs. III and IV using the data of the CENNS-10 analysis B in order to check the compatibility and stability of the results. These two different datasets are obtained from the same data-taking campaign and share most of the selection procedure, leading to have most of the data in common. Thus, any attempt to combine the results of analyses A and B in order to obtain a more precise measurement of the physics parameters should be discarded, given the large overlap between the two.

In contrast to analysis A, the slightly different selection in analysis B results in a modified efficiency that is below the efficiency of analysis A except for a small region between 4 keV$_{ee}$ and 5 keV$_{ee}$. In addition, the region of interest of analysis B is restricted to [4, 30] keV$_{ee}$, which corresponds roughly to the CEνNS signal energy region. The results are presented using 13 bins of 2 keV$_{ee}$ each. Another difference is that, in analysis B, the delayed component of BRN is not included, and thus the background has a single component, B^{BRN}. The least-squares function becomes

$$\chi^2_{\mathrm{S}} = \sum_{i=1}^{13} \left(\frac{N_i^{\mathrm{exp}} - \eta_{\mathrm{CE}\nu\mathrm{NS}} N_i^{\mathrm{CE}\nu\mathrm{NS}} - \eta_{\mathrm{BRN}} B_i^{\mathrm{BRN}}}{\sigma_i} \right)^2 + \left(\frac{\eta_{\mathrm{CE}\nu\mathrm{NS}} - 1}{\sigma_{\mathrm{CE}\nu\mathrm{NS}}} \right)^2 + \left(\frac{\eta_{\mathrm{BRN}} - 1}{\sigma_{\mathrm{BRN}}} \right)^2, \tag{A1}$$

with

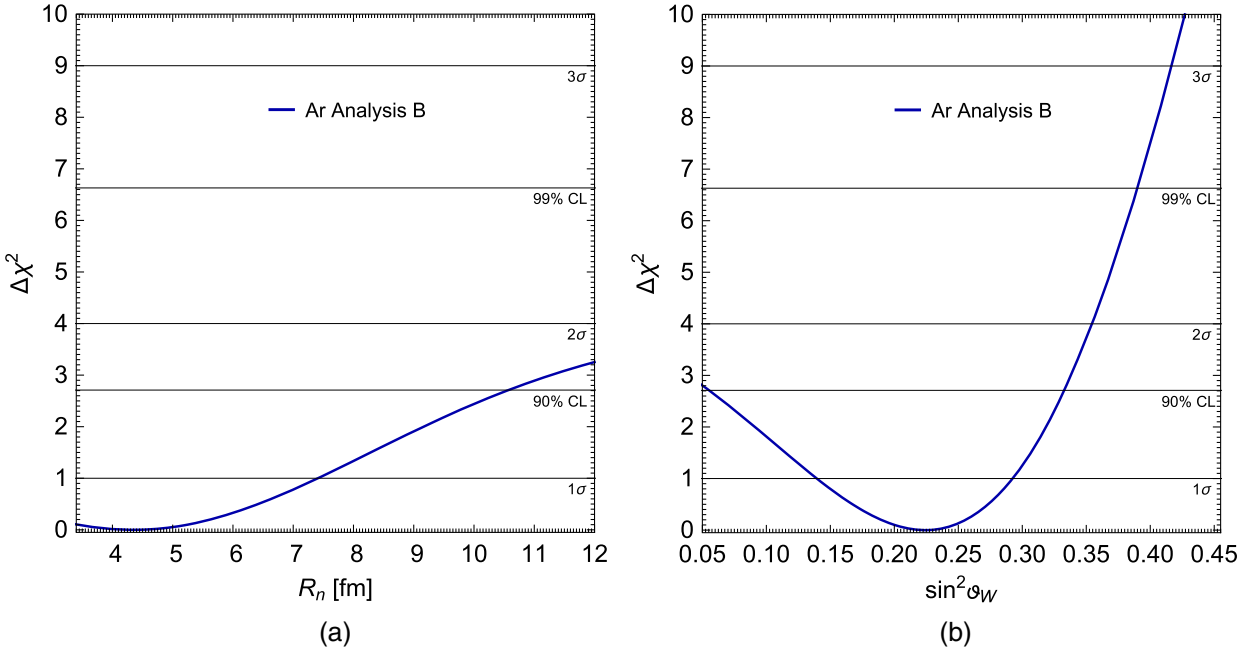

FIG. 10. $\Delta\chi^2$ profiles for the CENNS-10 analysis B as (a) a function of the neutron rms radius R_n, fixing the value of the weak mixing angle $\sin^2\vartheta_W = 0.23587$, and (b) of $\sin^2\vartheta_W$, fixing the value of R_n.

$$\sigma_i^2 = (\sigma_i^{\mathrm{exp}})^2 + [\sigma_{\mathrm{BRNES}} B_i^{\mathrm{BRN}}]^2, \tag{A2}$$

$$\sigma_{\mathrm{BRNES}} = \sqrt{\frac{0.052^2}{13}} = 1.4\%, \tag{A3}$$

$$\sigma_{\mathrm{CE}\nu\mathrm{NS}} = 12\%, \tag{A4}$$

$$\sigma_{\mathrm{BRN}} = 14.6\%, \tag{A5}$$

where these quantities have been introduced in Sec. III. We notice that the systematic uncertainties of analysis B are smaller with respect to analysis A and the energy resolution is better. On the other hand, since the selection performed in analysis B is tighter, the number of expected CEνNS events is smaller and the resulting uncertainty is larger than analysis A. Fixing the value of the weak mixing angle to the SM one, $\sin^2\vartheta_W = 0.23857$ [21], and fitting the radius of the nuclear neutron distribution R_n, constraining it to be $R_n > R_p$, we find

$$R_n(^{40}\mathrm{Ar}) < 7.4(1\sigma), 10.55(90\%\ \mathrm{C.L.})\ \mathrm{fm}. \tag{A6}$$

Figure 10(a) shows the $\Delta\chi^2$ as a function of the neutron rms radius R_n for analysis B. Even though a minimum is found at $R_n = 4.36$ fm, the large uncertainty allows one to set limits only on the neutron rms radius, which are much weaker than those obtained with the analysis A.

Similarly, we determined the value of $\sin^2\vartheta_W$ fixing R_n. This choice does not impact significantly the result, since it has been verified that the extracted value of the weak mixing angle is largely uncorrelated with R_n. Under these assumptions, we obtain

$$\sin^2\vartheta_W = 0.22^{+0.07}_{-0.09}(1\sigma)^{+0.11}_{-0.17}(90\%\ \mathrm{C.L.}). \tag{A7}$$

This value is consistent with the SM prediction and with the best fit obtained using analysis A, but a much larger uncertainty is obtained.[2] Figure 10(b) shows the $\Delta\chi^2$ as a function of the weak mixing angle for analysis B.

[2]To better judge the consistency one should know the overlap, in terms of the number of events, between the two analyses, but this information is missing in Ref. [13].

[1] D. Akimov *et al.* (COHERENT Collaboration), Science **357**, 1123 (2017).
[2] D. Akimov *et al.* (COHERENT Collaboration), arXiv:1804.09459.
[3] M. Cadeddu, C. Giunti, Y. F. Li, and Y. Y. Zhang, Phys. Rev. Lett. **120**, 072501 (2018).
[4] D. K. Papoulias, T. S. Kosmas, R. Sahu, V. K. B. Kota, and M. Hota, Phys. Lett. B **800**, 135133 (2020).
[5] P. Coloma, M. C. Gonzalez-Garcia, M. Maltoni, and T. Schwetz, Phys. Rev. D **96**, 115007 (2017).
[6] J. Liao and D. Marfatia, Phys. Lett. B **775**, 54 (2017).
[7] D. K. Papoulias and T. S. Kosmas, Phys. Rev. D **97**, 033003 (2018).
[8] P. B. Denton, Y. Farzan, and I. M. Shoemaker, J. High Energy Phys. 07 (2018) 037.
[9] D. A. Sierra, V. De Romeri, and N. Rojas, Phys. Rev. D **98**, 075018 (2018).
[10] M. Cadeddu, C. Giunti, K. Kouzakov, Y. F. Li, A. Studenikin, and Y. Y. Zhang, Phys. Rev. D **98**, 113010 (2018).
[11] B. Dutta, S. Liao, S. Sinha, and L. E. Strigari, Phys. Rev. Lett. **123**, 061801 (2019).
[12] B. Dutta, D. Kim, S. Liao, J.-C. Park, S. Shin, and L. E. Strigari, Phys. Rev. Lett. **124**, 121802 (2020).
[13] D. Akimov *et al.* (COHERENT Collaboration), arXiv:2003.10630.
[14] V. A. Bednyakov and D. V. Naumov, Phys. Rev. D **98**, 053004 (2018).
[15] M. Cadeddu, F. Dordei, C. Giunti, Y. Li, and Y. Zhang, Phys. Rev. D **101**, 033004 (2020).
[16] O. G. Miranda, D. K. Papoulias, G. S. Garcia, O. Sanders, M. Tortola, and J. W. F. Valle, J. High Energy Phys. 05 (2020) 130.
[17] A. Drukier and L. Stodolsky, Phys. Rev. D **30**, 2295 (1984).
[18] J. Barranco, O. G. Miranda, and T. I. Rashba, J. High Energy Phys. 12 (2005) 021.
[19] K. Patton, J. Engel, G. C. McLaughlin, and N. Schunck, Phys. Rev. C **86**, 024612 (2012).
[20] J. Erler and S. Su, Prog. Part. Nucl. Phys. **71**, 119 (2013).
[21] M. Tanabashi *et al.* (Particle Data Group), Phys. Rev. D **98**, 030001 (2018).
[22] J. Alitti *et al.* (UA2 Collaboration), Phys. Lett. B **263**, 563 (1991).
[23] J. Bernabeu, L. G. Cabral-Rosetti, J. Papavassiliou, and J. Vidal, Phys. Rev. D **62**, 113012 (2000).
[24] J. Bernabeu, J. Papavassiliou, and J. Vidal, Phys. Rev. Lett. **89**, 101802 (2002).
[25] J. Bernabeu, J. Papavassiliou, and J. Vidal, Nucl. Phys. **B680**, 450 (2004).
[26] J. Piekarewicz, A. R. Linero, P. Giuliani, and E. Chicken, Phys. Rev. C **94**, 034316 (2016).
[27] R. H. Helm, Phys. Rev. **104**, 1466 (1956).
[28] S. Klein and J. Nystrand, Phys. Rev. C **60**, 014903 (1999).
[29] A. N. Khan and W. Rodejohann, Phys. Rev. D **100**, 113003 (2019).
[30] D. K. Papoulias, arXiv:1907.11644.
[31] J. Friedrich and N. Voegler, Nucl. Phys. **A373**, 192 (1982).
[32] G. Fricke, C. Bernhardt, K. Heilig, L. A. Schaller, L. Schellenberg, E. B. Shera, and C. W. de Jager, At. Data Nucl. Data Tables **60**, 177 (1995).
[33] I. Angeli and K. P. Marinova, At. Data Nucl. Data Tables **99**, 69 (2013).
[34] A. Ong, J. C. Berengut, and V. V. Flambaum, Phys. Rev. C **82**, 014320 (2010).
[35] C. J. Horowitz *et al.*, Phys. Rev. C **85**, 032501 (2012).
[36] H.-W. Hammer and U.-G. Meißner, Sci. Bull. **65**, 257 (2020).
[37] C. G. Payne, S. Bacca, G. Hagen, W. Jiang, and T. Papenbrock, Phys. Rev. C **100**, 061304 (2019).
[38] J. A. Maruhn, P. G. Reinhard, P. D. Stevenson, and A. S. Umar, Comput. Phys. Commun. **185**, 2195 (2014).
[39] T. Niksic, N. Paar, D. Vretenar, and P. Ring, Comput. Phys. Commun. **185**, 1808 (2014).
[40] P. G. Reinhard and H. Flocard, Nucl. Phys. **A584**, 467 (1995).
[41] E. Chabanat, P. Bonche, P. Haensel, J. Meyer, and R. Schaeffer, Nucl. Phys. **A635**, 231 (1998).
[42] K.-H. Kim, T. Otsuka, and P. Bonche, J. Phys. G **23**, 1267 (1997).
[43] P. Klupfel, P. G. Reinhard, T. J. Burvenich, and J. A. Maruhn, Phys. Rev. C **79**, 034310 (2009).
[44] M. Kortelainen, T. Lesinski, J. More, W. Nazarewicz, J. Sarich, N. Schunck, M. V. Stoitsov, and S. Wild, Phys. Rev. C **82**, 024313 (2010).
[45] M. Kortelainen, J. McDonnell, W. Nazarewicz, P. G. Reinhard, J. Sarich, N. Schunck, M. V. Stoitsov, and S. M. Wild, Phys. Rev. C **85**, 024304 (2012).
[46] J. Bartel, P. Quentin, M. Brack, C. Guet, and H. B. Hakansson, Nucl. Phys. **A386**, 79 (1982).
[47] J. Dobaczewski, H. Flocard, and J. Treiner, Nucl. Phys. **A422**, 103 (1984).
[48] T. Niksic, D. Vretenar, P. Finelli, and P. Ring, Phys. Rev. C **66**, 024306 (2002).
[49] T. Niksic, D. Vretenar, and P. Ring, Phys. Rev. C **78**, 034318 (2008).
[50] E. Ciuffoli, J. Evslin, Q. Fu, and J. Tang, Phys. Rev. D **97**, 113003 (2018).
[51] M. Safronova, D. Budker, D. DeMille, D. F. J. Kimball, A. Derevianko, and C. W. Clark, Rev. Mod. Phys. **90**, 025008 (2018).
[52] J. I. Collar, A. R. L. Kavner, and C. M. Lewis, Phys. Rev. D **100**, 033003 (2019).
[53] M. Bender, K. Rutz, P.-G. Reinhard, J. A. Maruhn, and W. Greiner, Phys. Rev. C **60**, 034304 (1999).
[54] C. S. Wood, S. C. Bennett, D. Cho, B. P. Masterson, J. L. Roberts, C. E. Tanner, and C. E. Wieman, Science **275**, 1759 (1997).
[55] V. A. Dzuba, J. C. Berengut, V. V. Flambaum, and B. Roberts, Phys. Rev. Lett. **109**, 203003 (2012).
[56] P. L. Anthony *et al.* (SLAC E158 Collaboration), Phys. Rev. Lett. **95**, 081601 (2005).
[57] D. Wang *et al.* (PVDIS Collaboration), Nature (London) **506**, 67 (2014).
[58] G. P. Zeller *et al.* (NuTeV Collaboration), Phys. Rev. Lett. **88**, 091802 (2002).
[59] D. Androic *et al.* (Qweak Collaboration), Nature (London) **557**, 207 (2018).
[60] C. Giunti and A. Studenikin, Rev. Mod. Phys. **87**, 531 (2015).

[61] K. A. Kouzakov and A. I. Studenikin, Phys. Rev. D **95**, 055013 (2017); **96**, 099904(E) (2017).
[62] A. Grau and J. Grifols, Phys. Lett. B **166B**, 233 (1986).
[63] G. Degrassi, A. Sirlin, and W. J. Marciano, Phys. Rev. D **39**, 287 (1989).
[64] P. Vogel and J. Engel, Phys. Rev. D **39**, 3378 (1989).
[65] C. Giunti and C. W. Kim, in *Fundamentals of Neutrino Physics and Astrophysics* (Oxford University Press, Oxford, UK, 2007), pp. 1–728.
[66] M. Deniz *et al.* (TEXONO Collaboration), Phys. Rev. D **81**, 072001 (2010).
[67] L. Ahrens, S. Aronson, P. Connolly, B. Gibbard, M. Murtagh *et al.*, Phys. Rev. D **41**, 3297 (1990).
[68] A. Studenikin, Europhys. Lett. **107**, 21001 (2014); **107**, 39901(E) (2014).
[69] J.-W. Chen, H.-C. Chi, H.-B. Li, C. P. Liu, L. Singh, H. T. Wong, C.-L. Wu, and C.-P. Wu (TEXONO Collaboration), Phys. Rev. D **90**, 011301 (2014).
[70] C. Giunti, K. A. Kouzakov, Y.-F. Li, A. V. Lokhov, A. I. Studenikin *et al.*, Ann. Phys. (Berlin) **528**, 198 (2016).
[71] O. Miranda, D. Papoulias, M. Tortola, and J. W. F. Valle, J. High Energy Phys. 07 (**2019**) 103.
[72] D. Papoulias, T. Kosmas, and Y. Kuno, Front. Phys. **7**, 191 (2019).
[73] L. B. Auerbach *et al.* (LSND Collaboration), Phys. Rev. D **63**, 112001 (2001).
[74] A. G. Beda, V. B. Brudanin, V. G. Egorov, D. V. Medvedev, V. S. Pogosov, M. V. Shirchenko, and A. S. Starostin, Adv. High Energy Phys. **2012**, 350150 (2012).